

# Subvoxel Processing: A Method for Reducing Partial Volume Blurring With Application to In Vivo MR Images of Trabecular Bone

Scott N. Hwang and Felix W. Wehrli\*

**Partial volume blurring precludes accurate measurement of structural dimensions in the limited-resolution regime in which image voxel size is larger than the typical structural element to be resolved. Since acquiring images at increased resolution often exacts an unacceptable signal-to-noise ratio (SNR) penalty, methods to alleviate the adverse effects of partial volume blurring are instrumental for the accurate measurement of architectural parameters in applications such as predicting the mechanical competence of trabecular bone networks. In the current work, a novel post-processing method, referred to as “subvoxel processing,” is described for increasing apparent image resolution. The method is applicable to volumes of interest containing material phases of two discrete signal intensities. The principal strategy consists of subdividing voxels and assigning voxel intensities to each subvoxel on the basis of local neighborhood criteria and strict mass conservation. In the current work, the method’s accuracy has been evaluated using microcomputed tomography images ( $22 \times 22 \times 22 \mu\text{m}^3$  voxel size) of human trabecular bone. The results demonstrate that subvoxel processing is significantly more accurate than trilinear interpolation in decreasing apparent voxel size, especially in the presence of noise. In addition, the method’s effectiveness is illustrated with MR images of human trabecular bone acquired in vivo at  $137 \times 137 \times 350 \mu\text{m}^3$  voxel size. The subvoxel-processed images are shown to have architectural features characteristic of images acquired at higher spatial resolution. Magn Reson Med 47:948–957, 2002. © 2002 Wiley-Liss, Inc.**

**Key words:** image processing; resolution enhancement; trabecular bone architecture; quantitative microimaging; partial volume blurring

MRI is a powerful tool for noninvasively quantifying tissue morphology. However, when voxel size is larger than the structures of interest, partial volume blurring complicates the accurate measurement of structural parameters. On the other hand, acquisition of images at higher resolution often exacts an unacceptable signal-to-noise ratio (SNR) penalty, and thus does not represent a viable alternative. For example, these constraints have been the major obstacle to the development of MRI as a means of quantifying trabecular bone architecture in vivo for the purpose of predicting fracture risk in osteopenic subjects (1–4). As trabecular thickness (80–150  $\mu\text{m}$ ) is typically less than the achiev-

able voxel size in vivo ( $\sim 150 \mu\text{m}$ ), accurate structural information is difficult to obtain. The common approach toward quantifying trabecular structure has been to classify voxels as either “bone” or “marrow” via binary segmentation. In the low-spatial-resolution regime, however, the “bone” voxels contain varying amounts of bone, usually with a higher proportion of marrow. In order to avoid the loss of information inherent in binary classification, a means of estimating the bone volume fraction (BVF) in each voxel (5) was devised. The logical extension of this method, referred to as BVF mapping, would be to apply an algorithm for increasing the apparent resolution of the BVF map.

Linear interpolation has commonly been applied to increase the apparent resolution of digital images. In one dimension, for example, BVF at a spatial location between the centers of two adjacent voxels would be computed as the average of the two voxels. Therefore, additional values calculated in this manner will never increase beyond the original values, and thus contradict the axiom that smaller voxels are more likely to contain larger fractions of bone. In the current work, a method is presented for increasing the apparent image resolution. The method is illustrated with images of trabecular bone; however, the algorithm may easily be applied to images of other materials, which may be considered to locally contain only two phases. The method is related to the method of Bayesian subvoxel classification (6), which also divides voxels into subvoxels. However, with the latter method, the output is a binarized image, i.e., the subvoxels are constrained to contain either 100% bone or 100% marrow. In contrast, subvoxel processing assigns partial fractions to each subvoxel (7).

## THEORY

### Single-Pass Subvoxel Processing

Subvoxel processing is an empirical algorithm (rather than one derived from mathematical theory), and is based on two assumptions: 1) smaller voxels are more likely to have high BVF, and 2) bone is generally in close proximity to more bone. The starting point of the algorithm is the partitioning of each voxel into eight subvoxels by strictly enforcing conservation of bone mass, i.e., the total BVF in the original voxel is divided among the subvoxels. The precise amount allotted to a subvoxel is determined by the amount and location of bone outside the voxel but adjacent to the subvoxel. Thus, bone tends to be sequestered in the area of the voxel that is closest to other bone.

The images subjected to subvoxel processing are assumed to be BVF maps, i.e., the value of each voxel is equal to the volume fraction occupied by bone. Since

Laboratory for Structural NMR Imaging, Department of Radiology, University of Pennsylvania Medical Center, Philadelphia, Pennsylvania.

A preliminary account of this work was presented at the 8th Annual Meeting of ISMRM, Denver, 2000.

Grant sponsor: National Institutes of Health; Grant numbers: RO1 41443; RO1 40671.

\*Correspondence to: Felix W. Wehrli, Ph.D., Department of Radiology, University of Pennsylvania Medical Center, 3400 Spruce St., Philadelphia, PA 19104. E-mail: wehrli@oasis.rad.upenn.edu

Received 27 February 2001; revised 14 January 2002; accepted 14 January 2002.

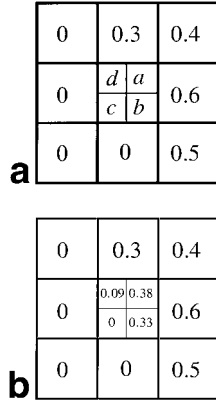


FIG. 1. **a:** An array of voxels in which the central voxel has been partitioned into subvoxels *a–d*. **b:** The computed BVFs of the subvoxels are shown assuming that the BVF of the central voxel was 0.20. Note that the average of the subvoxel BVFs (i.e.,  $[0.38 + 0.33 + 0 + 0.09]/4$ ) is still 0.20, in accordance with the condition that total mass be conserved.

protons in bone have very short transverse relaxation times, their signal is not ordinarily detected. Thus, bone appears with background intensity in MR images and, in the absence of noise, voxel intensity is proportional to marrow volume fraction (MVF). Although MR images are actually images of marrow, not bone, bone is the material of primary interest in regard to predicting the mechanical competence of trabecular bone; therefore, processing of the images has been discussed and defined in terms of BVF. Since images of trabecular bone may be considered as containing only marrow and bone,  $BVF = 1 - MVF$ , and MVF maps may be converted to BVF maps without loss or corruption of information.

The principle of subvoxel processing is illustrated in two dimensions with a  $3 \times 3$  array of voxels in which the central voxel ( $BVF = 0.2$ ) has been partitioned into four subvoxels (Fig. 1a). The weight for a subvoxel is computed as the sum of the BVFs from all the voxels adjacent to the subvoxel. For the example, the weight for subvoxel *a* is obtained as the sum of the three adjacent voxel BVFs (i.e.,  $0.3 + 0.4 + 0.6 = 1.3$ ). Similarly, the weights for subvoxels *b*, *c*, and *d* are 1.1, 0, and 0.3, respectively. In general, the number of adjacent voxels is  $2^N - 1$ , where  $N$  is the dimensionality of the image array.

To explicitly define the subvoxel weights, let  $(x, y)$ , where  $x = 0, 1, 2, \dots, xres-1$  and  $y = 0, 1, 2, \dots, yres-1$ , represent the indices of the voxel being processed in an array of resolution  $xres \times yres$ . Each subvoxel is referenced by an integer  $s$ , ranging from 0 to  $2^N - 1$  (Fig. 2). The  $2^N - 1$  offsets  $(vx_{s,n}, vy_{s,n})$  for localizing the neighboring voxels in reference to the voxel containing subvoxel  $s$  are shown in Table 1, where  $n = 0$  to  $2^N - 2$ . The subvoxel weights  $w_s$  are then computed as:

$$w_{\text{subvoxel},s}(x, y) = \sum_{n=0}^{2^N-2} BVF_{\text{voxel}}(x + vx_{s,n}, y + vy_{s,n}) \quad [1]$$

where  $BVF_{\text{voxel}}(x, y)$  is the voxel BVF at  $(x, y)$ . The weights for a 3D voxel are computed in similar manner with the 3D offsets  $(vx_{s,n}, vy_{s,n}, vz_{s,n})$  shown in Table 2.

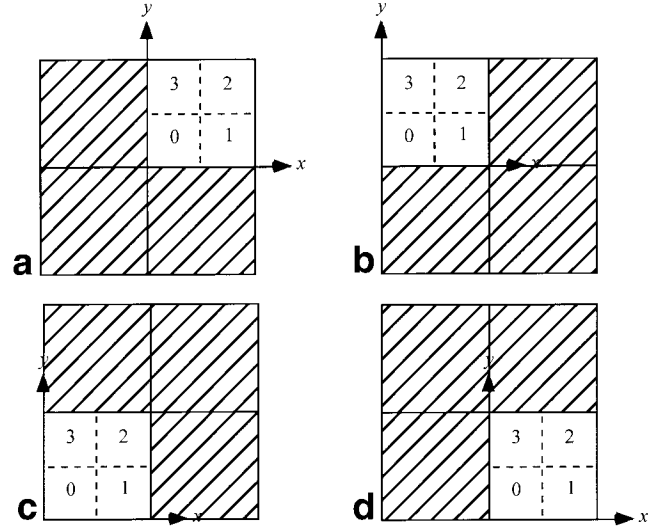


FIG. 2. The neighboring voxels applied to compute the weights for each of the subvoxels in a 2D voxel. The dashed lines partition the 2D voxel into the subvoxels, which are labeled 0–3. The hatched voxels in **a–d** represent the voxels whose intensities are summed to compute the weight for subvoxels 0–3, respectively. The coordinate offsets for the hatched voxels are shown in Table 1.

The bone is then partitioned among the subvoxels according to their fractional weights, which may be computed as  $w_{s_i}/w_{\text{total}}$ , where  $w_{\text{total}}$  is the total sum of weights:

$$w_{\text{total}} = \sum_{s=0}^{s=2^N-1} w_{\text{subvoxel},s}. \quad [2]$$

The absolute volume of bone in the voxel,  $BV_{\text{voxel}}$ , is equal to the product of  $BVF_{\text{voxel}}$ , the bone volume fraction of the voxel, and  $V_{\text{voxel}}$ , the volume of the voxel. To enforce conservation of bone mass, the volume of bone allotted to a subvoxel,  $BV_{\text{subvoxel},i}$ , may be assumed to be:

$$BV_{\text{subvoxel},s} = \frac{w_{\text{subvoxel},s}}{w_{\text{total}}} \times BV_{\text{voxel}}. \quad [3]$$

Note that

$$\sum_{s=0}^{s=2^N-1} BV_{\text{subvoxel},s} = \sum_{s=0}^{s=2^N-1} \frac{w_{\text{subvoxel},s}}{w_{\text{total}}} BV_{\text{voxel}} = BV_{\text{voxel}}, \quad [4]$$

demonstrating that the amount of bone is conserved. Subsequently, the subvoxel BVF is given by

Table 1  
Voxel Offsets  $(vx, vy)$  for Computing the Weights for Subvoxels 0 Through 3 in a 2D Voxel

Subvoxel 0	Subvoxel 1	Subvoxel 2	Subvoxel 3
(-1, -1)	(1, -1)	(1, 1)	(-1, 1)
(-1, 0)	(1, 0)	(1, 0)	(-1, 0)
(0, -1)	(0, -1)	(0, 1)	(0, 1)

Table 2  
Voxel Offsets ( $v_x, v_y, v_z$ ) for Computing the Weights for Subvoxels 0 Through 7 in a 3D Voxel

Subvoxel 0	Subvoxel 1	Subvoxel 2	Subvoxel 3	Subvoxel 4	Subvoxel 5	Subvoxel 6	Subvoxel 7
(-1, -1, -1)	(1, -1, -1)	(1, 1, -1)	(-1, 1, -1)	(-1, -1, 1)	(1, -1, 1)	(1, 1, 1)	(-1, 1, 1)
(-1, -1, 0)	(1, -1, 0)	(1, 1, 0)	(-1, 1, 0)	(-1, -1, 0)	(1, -1, 0)	(1, 1, 0)	(-1, 1, 0)
(-1, 0, 1)	(1, 0, -1)	(1, 0, -1)	(-1, 0, -1)	(-1, 0, 1)	(1, 0, 1)	(1, 0, 1)	(-1, 0, 1)
(-1, 0, 0)	(1, 0, 0)	(1, 0, 0)	(-1, 0, 0)	(-1, 0, 0)	(1, 0, 0)	(1, 0, 0)	(-1, 0, 0)
(0, -1, -1)	(0, -1, -1)	(0, 1, -1)	(0, 1, -1)	(0, -1, 1)	(0, -1, 1)	(0, 1, 1)	(0, 1, 1)
(0, -1, 0)	(0, -1, 0)	(0, 1, 0)	(0, 1, 0)	(0, -1, 0)	(0, -1, 0)	(0, 1, 0)	(0, 1, 0)
(0, 0, -1)	(0, 0, -1)	(0, 0, -1)	(0, 0, -1)	(0, 0, 1)	(0, 0, 1)	(0, 0, 1)	(0, 0, 1)

$$\begin{aligned} \text{BVF}_{\text{subvoxel},s} &= \frac{\text{BV}_{\text{subvoxel},s}}{V_{\text{subvoxel}}} = \frac{W_{\text{subvoxel},s}}{W_{\text{total}}} \times \text{BVF}_{\text{voxel}} \\ &\times \frac{V_{\text{voxel}}}{V_{\text{subvoxel}}} = \frac{W_{\text{subvoxel},s}}{W_{\text{total}}} \times \text{BVF}_{\text{voxel}} \times 2^N. \end{aligned} \quad [5]$$

Note that the product  $\text{BVF}_{\text{voxel}} \times 2^N$  is equal to the sum of BVF from all the subvoxels in the voxel. For the example in Fig. 1, the sum of weights is 2.7. Thus,  $1.3/2.7 = 0.48$  of the bone volume is allotted to subvoxel  $a$ , yielding a BVF of  $0.48 \times 0.2 \times 4 = 0.38$ .

If voxel BVF is high, a subvoxel may be assigned an unrealistic  $\text{BVF} > 1$  because the subvoxels are smaller than the original voxel. For example, if the center voxel had a BVF of 0.9, the resulting  $\text{BVF}_{\text{subvoxel}}$  for  $a$  would be 1.7. In such a case, the subvoxel is assigned a BVF of 1 and the residual bone is partitioned among the other subvoxels according to the remaining weights. Therefore, for each voxel, the algorithm processes each subvoxel in order of decreasing weight. The BVF assigned to each subvoxel is determined from the subvoxel's weight and then subtracted from the remaining bone in the voxel. To express this algorithm mathematically, each subvoxel in a voxel may be referenced by the subscript  $n$ , where  $n$  is an integer ranging from 0 through  $2^N-1$ . The subscript  $n$  differs from  $s$  in that  $n$  references each subvoxel in order of decreasing weight such that subvoxel  $n$  must have a weight less than or equal to subvoxel  $n-1$ . If the residual sum of BVF is defined as

$$\text{BVF}_{\text{residual},n} = 2^N \times \text{BVF}_{\text{voxel}} - \sum_{i=0}^{n-1} \text{BVF}_{\text{subvoxel},i} \quad [6]$$

then the residual BVF for the first voxel is  $\text{BVF}_{\text{residual},0} = 2^N \times \text{BVF}_{\text{voxel}}$ , the product that was noted in Eq. [5] as the sum of BVF from all the subvoxels in the voxel. A residual sum of unprocessed subvoxel weights is also expressed as

$$W_{\text{total},n} = \sum_{i=n}^{2^N-1} W_{\text{subvoxel},i}. \quad [7]$$

Subvoxel BVF is then given as in Eq. [5], except that the sums of subvoxel BVF and of the weights are replaced by the residual sums of BVF and the weights. In addition, the minimum function,  $\min(a,b)$ , which returns the lesser of  $a$  and  $b$ , is applied to restrict BVF to values  $\leq 1$ :

$$\text{BVF}_{\text{subvoxel},n} = \min\left(1, \frac{W_{\text{subvoxel},n}}{W_{\text{total},n}} \times \text{BVF}_{\text{residual},n}\right). \quad [8]$$

#### Multiple-Pass Algorithm

Trabeculae may still become artifactually diffuse with the single-pass algorithm. For example, consider the 2D trabeculae represented by the array of voxels in Fig. 3a. After applying the single-pass subvoxel algorithm (Fig. 3c), bone

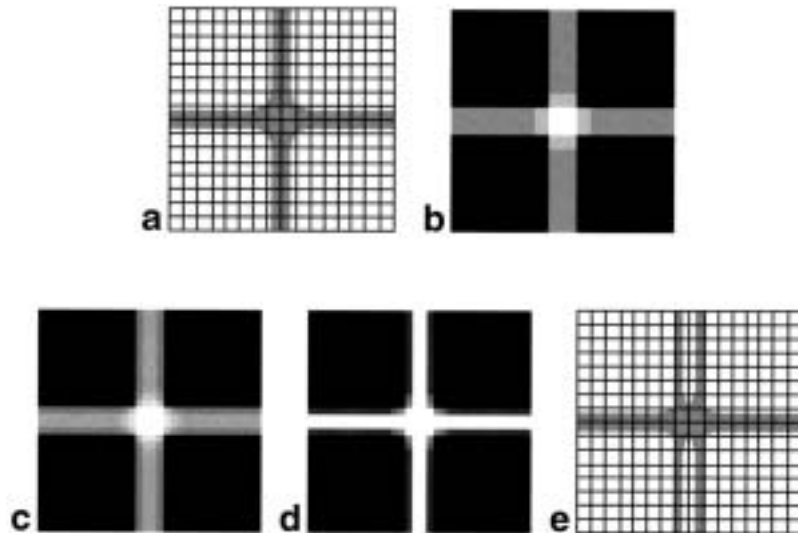


FIG. 3. Multi-pass processing. **a**: Intersecting trabeculae (gray) partially filling two rows and two columns in an array of voxels delineated by the solid lines. **b**: A BVF map of the array in part **a**, in which increased intensity indicates higher BVF (e.g., black and white indicate  $\text{BVF} = 0$  and  $\text{BVF} = 1$ , respectively). **c**: Although single-pass subvoxel processing allocates more bone to the central subvoxels, none of them contain 100% bone. **d**: After second-pass processing, the central subvoxels have been correctly assigned  $\text{BVF} = 1$ . **e**: The BVF map in part **b** would be identical if the vertical trabecula were replaced by multiple thin trabeculae (e.g., two trabeculae of half thickness) within the same two columns of voxels. It is assumed that the image resolution is high enough that the simpler structure with a single trabecula is the correct solution.

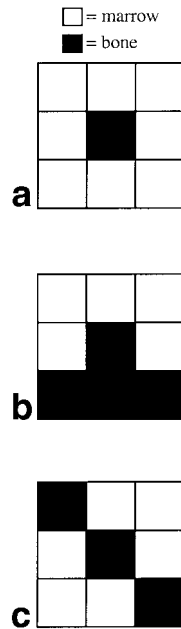


FIG. 4. Local connectivity for a central bone voxel (black) is defined as the number of objects a particular pixel *might* connect, judging from its eight nearest neighbors (26 neighbors in 3D). The connectivity may be obtained by counting the number of isolated “islands” of bone generated by reclassifying the central voxel as marrow. **a**: Connectivity = 0. Reclassifying the central voxel does not disconnect any regions. **b**: Connectivity = 1. **c**: Connectivity = 2. Reclassification of the central voxel apparently disconnects the bone voxels in the corners even though they might still be connected outside the local neighborhood.

has been preferentially allocated towards the central rows of subvoxels, but none of them contain 100% bone. If it is assumed that the original spatial resolution is high enough that there are no voxels that contain more than one trabecula, only subvoxels that are on the boundary of a trabecula should contain partial fractions of both bone and marrow. Blurred trabeculae may be completely eliminated to produce a more compact solution by application of a multiple-pass algorithm. Subvoxels are classified as boundary or central subvoxels on the basis of the output of the first-pass algorithm. During subsequent passes, boundary subvoxels are not assigned bone until the central voxels contain 100% bone (Fig. 3d). If image resolution is low, the assumption of no more than one trabecula in each voxel may be violated. Given a single voxel that contains partial volumes of both bone and marrow, it is impossible to know how many trabeculae are within the voxel. For example, if it is known that a voxel is 20% bone, there could be two trabeculae, each of which occupies 10% of the voxel, or four trabeculae, each of which occupies 5% of the voxel. The BVF map in Fig. 3b would be identical if the vertical trabecula were replaced by multiple thinner trabeculae (e.g., by two trabeculae of half the original thickness) passing through the same two columns of voxels (Fig. 3e). Subvoxel processing would then, of course, result in an incorrect solution. However, at the current in vivo voxel size of  $137 \times 137 \times 350 \mu\text{m}^3$ , and considering average trabecular thicknesses and intertrabecular spac-

ings of 100 and 500–1000  $\mu\text{m}$ , respectively, the occurrence of multiple trabeculae within a single voxel is highly unlikely.

In the multiple-pass algorithm, bone-containing subvoxels are classified as boundary or central subvoxels on the basis of adjacency and connectivity criteria. The adjacency criterion requires that one of the subvoxel’s six nearest neighbors in 3D (four nearest neighbors in 2D) does not contain bone. A boundary subvoxel also must not be critical to the trabecular network as quantified by local connectivity. The local connectivity is computed on the basis of the  $2^N-1$  nearest-neighbor previous-pass subvoxels. The connectivity is equal to the number of “islands” of bone that are generated in the local neighborhood by temporarily assuming the central subvoxel contains marrow only (Fig. 4). If the edge subvoxel has a connectivity of  $<2$ , its bone may be shifted to another voxel without damaging the connectivity of the network, and may thus be classified as a boundary voxel. Subvoxels, which do not satisfy both of these criteria, are classified as central subvoxels.

Central subvoxels are preferentially filled with bone by assigning subvoxels primary and secondary weights. Boundary voxels that are not critical to the trabecular network are assigned a primary weight of zero. Bone is then partitioned among the subvoxels on the basis of the primary weights. After the subvoxels with non-zero primary weights have been assigned bone, the remaining bone is partitioned among the subvoxels, which have not been assigned a BVF, according to the secondary weights. Weights may be computed as the weights in the single-pass algorithm. However, the current implementation of the algorithm further compacts the bone by calculating the secondary weights as the sum of the BVFs of the  $2^N-1$  first-pass subvoxels whose locations are adjacent to that of the second-pass subvoxel but outside the voxel (Fig. 5):

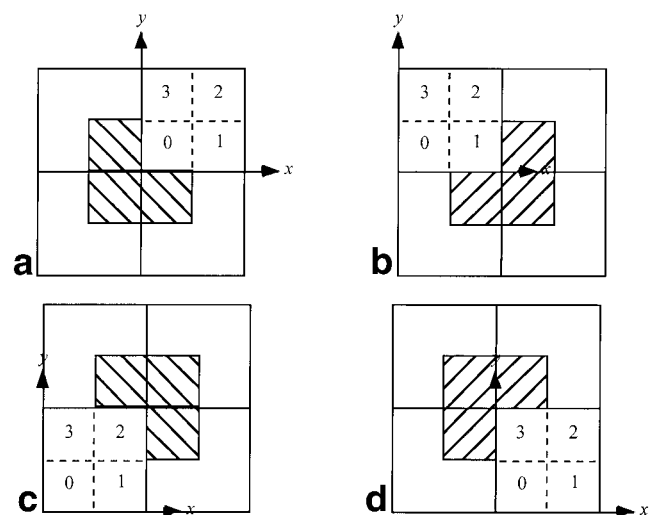


FIG. 5. The neighboring subvoxels applied to compute the weights for each of the subvoxels in a 2D voxel after the first iteration in the multiple-pass algorithm. The hatched subvoxels in **a–d** represent the subvoxels whose intensities are summed to compute the weight for subvoxels 0–3, respectively.

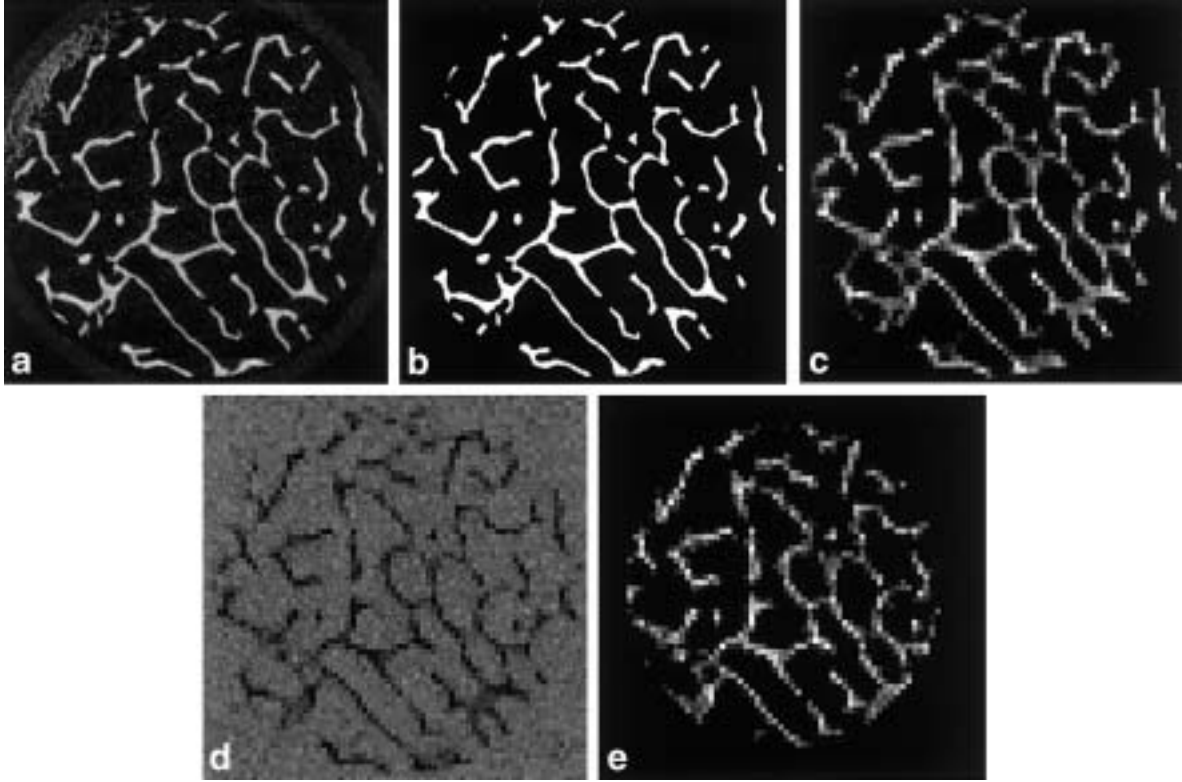


FIG. 6. **a**: One of 416 cross-sectional slices of the unprocessed 3D  $\mu$ -CT image ( $22 \times 22 \times 22 \mu\text{m}^3$  voxel size) of one of the human radius specimens. **b**: Cross section of the gold-standard BVF map ( $33 \times 33 \times 22 \mu\text{m}^3$  voxel size). Voxel intensity is proportional to BVF (i.e., black indicates no bone). **c**: Cross section of the noiseless low-resolution BVF map ( $132 \times 132 \times 352 \mu\text{m}^3$  voxel size, SNR = 10) **d**: Cross section of the test image ( $132 \times 132 \times 352 \mu\text{m}^3$  voxel size, SNR = 10) **e**: Cross section of the result of applying fast BVF mapping applied to the image in **d**.

$$w_{\text{secondary},s}(\mathbf{x}, y) = \sum_{n=0}^{2^N-2} \text{BVF}_{\text{subvoxel}}(2x + svx_s + vx_{s,n}, 2y + svy_s + vy_{s,n}), \quad [9]$$

where  $(svx_s, svy_s)$  is an additional offset for each subvoxel relative to subvoxel 0. For example, the offsets for subvoxels 0–3 for a 2D subvoxel are (0, 0), (1, 0), (1, 1), and (0, 1), respectively. The factors of 2 in the indices of  $\text{BVF}_{\text{subvoxel}}$  are necessary since there are twice as many subvoxels for each dimension. Central subvoxels only require primary weights, which are thus identical to the secondary weights. For the boundary subvoxels, the secondary weights are obtained in the same manner (Eq. [9]) but the primary weights are set to zero:

$$w_{\text{primary},s}(\mathbf{x}, y) = \begin{cases} w_{\text{secondary},s}(\mathbf{x}, y), & \text{subvoxel } s \text{ in voxel } (\mathbf{x}, y) \\ & \text{is a central subvoxel} \\ 0, & \text{subvoxel } s \text{ in voxel } (\mathbf{x}, y) \\ & \text{is a boundary subvoxel.} \end{cases} \quad [10]$$

As was done in the single-pass algorithm, subvoxels are sorted in order of decreasing primary weights, and those with the same primary weight are further sorted according to their secondary weights. Subvoxel BVFs are then com-

puted in a manner similar to the single-pass algorithm using the following modified definitions:

$$\text{BVF}_{\text{subvoxel},n} = \begin{cases} \min\left(1, \frac{w_{\text{primary},n}}{w_{\text{total},n}} \times \text{BVF}_{\text{residual},n}\right), & n < B \\ \min\left(1, \frac{w_{\text{secondary},n}}{w_{\text{total},n}} \times \text{BVF}_{\text{residual},n}\right), & n \geq B \end{cases} \quad [11]$$

$$w_{\text{total},n} = \begin{cases} \sum_{i=n}^{2^N-1} w_{\text{primary},i}, & n < B \\ \sum_{i=n}^{2^N-1} w_{\text{secondary},i}, & n \geq B \end{cases}, \quad [12]$$

where  $B$  is the index of the first subvoxel that is not a central subvoxel, i.e., the first voxel that has a zero primary weight.  $\text{BVF}_{\text{residual}}$  is defined as in Eq. [6]. Since only the central subvoxels have non-zero primary weights, the boundary subvoxels are not assigned any bone unless all the central subvoxels are assigned  $\text{BVF} = 1$  (Fig. 3d).

## METHODS

### Simulated In Vivo Test Images

Images for evaluating subvoxel processing were generated from six 3D  $\mu$ -CT images of a cylindrical human radius

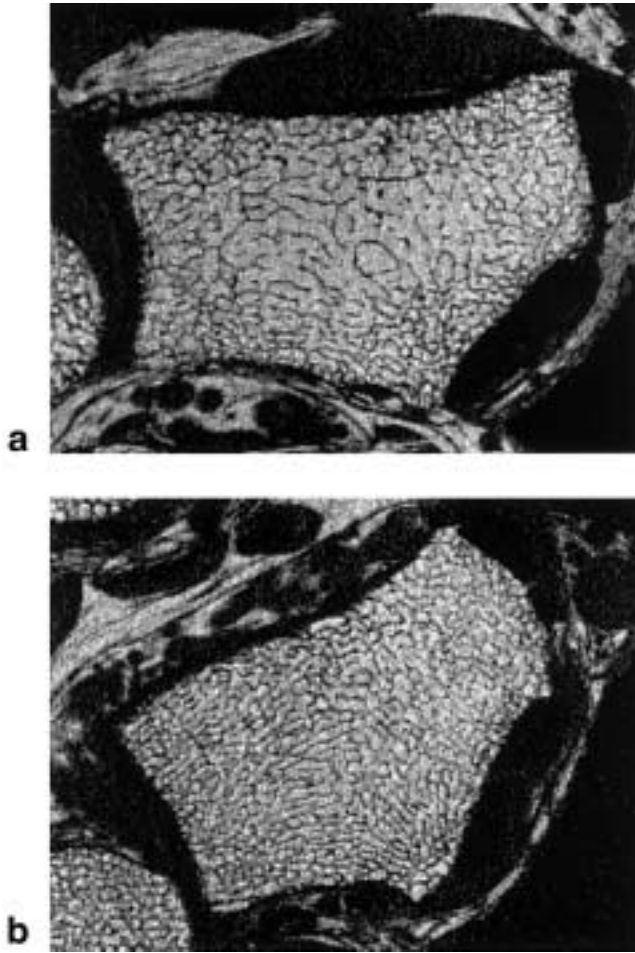


FIG. 7. Cross sections of the radius obtained from in vivo forearm images of (a) a 60-year-old (DEXA BMD L2-4 spine T-score = 0.3) and (b) a 63-year-old (T-score = 1.11) woman. The images were acquired at 1.5T using the fast large-angle spin-echo (FLASE) pulse sequence (11) at a voxel size of  $137 \times 137 \times 350 \mu\text{m}^3$ . The subject in part b has a higher number of trabeculae that are homogeneously distributed, while the subject in part a has thicker trabeculae, which are more numerous towards the periphery. In the current work, both data sets were subvoxel-processed and projected in 3D to highlight the differences in architecture.

specimen (Fig. 6a, 9 mm diameter and 9 mm length). The images were acquired with an MS-8 Volume Micro-CT system (Enhanced Visual Systems Corp., London, Canada) or a  $\mu$ -CT 20 scanner (Scanco Medical, Bassersdorf, Switzerland) at a voxel size of  $22 \times 22 \times 22 \mu\text{m}^3$ . They were then binarized with a classification threshold halfway between the marrow and bone peaks in the voxel intensity histogram. Subvoxel processing has been intended for application to in vivo MR forearm images, which are currently acquired with a voxel size of  $137 \times 137 \times 350 \mu\text{m}^3$ . Therefore, “gold standard” BVF maps (Fig. 6b) with a voxel size of  $33 \times 33 \times 22 \mu\text{m}^3$  were generated from each of the six specimens by interpolation such that increasing each voxel dimension by a factor of a power of 2 (i.e., a factor of 4 for the x and y dimensions, and a factor of 16 for the z direction) approximates the corresponding in vivo voxel dimension. Low-resolution BVF maps (Fig. 6c) were

subsequently created by averaging neighboring voxels ( $4 \times 4 \times 16$  voxels<sup>3</sup>) to yield a voxel size of  $132 \times 132 \times 352 \mu\text{m}^3$ .

To evaluate subvoxel processing in the presence of noise, simulated 3D MR images were generated (Fig. 7d). Since the MR signal from bone is negligible, the intensity of each voxel in the absence of noise is proportional to its marrow volume fraction (1-BVF):

$$I = (1 - \text{BVF}) \times I_{\text{marrow}} \quad [13]$$

where  $I_{\text{marrow}}$  is the intensity of a voxel that contains marrow only. In the current work,  $I_{\text{marrow}}$  was arbitrarily set to 100. Rician noise, the type of noise inherent to magnitude MR images (8), was added to simulate an SNR (defined as the ratio of the noise standard deviation in one Gaussian channel over the signal) of 10. Thus, both the resolution and the SNR were typical of in vivo MR images of the forearm (9).

#### Evaluation of Accuracy—Subvoxel Processing vs. Trilinear Interpolation

The accuracy of subvoxel processing was evaluated and compared with trilinear interpolation using the noiseless low-resolution BVF maps as input to the algorithms. Subvoxel processing was applied four times to each of the low-resolution BVF maps to return the voxel size to that of the gold standards. Each subvoxel processing iteration decreases voxel size by a factor of 2 in each dimension. Therefore, groups of four voxels ( $2 \times 2$  voxel<sup>2</sup>) were averaged in the x, y plane following the first and second iterations so that the overall voxel size was reduced by a factor of 4 in the x and y directions and by a factor of 16 in the z direction. The accuracy was assessed by generating histograms showing the fraction of subvoxels plotted vs. the error, computed as subvoxel BVF minus the spatially corresponding voxel BVF in the high-resolution gold standards. Quantitative parameters derived from the histograms include the fraction of subvoxels with zero error and the mean absolute error.

To evaluate the effect of noise on accuracy, subvoxel processing and trilinear interpolation were also applied to the test images with SNR = 10. Since subvoxel processing requires an estimate of the BVF in each voxel, the test images were first processed with a fast BVF mapping tech-

Table 3  
Comparison of Accuracy Between Subvoxel Processing and Linear Interpolation for Infinite SNR

Specimen	Subvoxel processing		Trilinear interpolation	
	Mean absolute error	% zero error	Mean absolute error	% zero error
1	0.064	86.7%	0.16	30.9%
2	0.070	86.6%	0.15	32.2%
3	0.056	87.7%	0.17	35.6%
4	0.038	91.8%	0.11	49.8%
5	0.078	84.7%	0.19	25.8%
6	0.063	86.1%	0.21	27.0%

Table 4  
Comparison of Accuracy Between Subvoxel Processing and Linear Interpolation for SNR = 10

Specimen	Subvoxel processing		Trilinear interpolation	
	Mean absolute error	% zero error	Mean absolute error	% zero error
1	0.092	83.4%	0.18	3.9%
2	0.090	83.9%	0.17	4.0%
3	0.078	84.5%	0.19	4.0%
4	0.055	89.5%	0.14	5.1%
5	0.099	81.8%	0.21	3.3%
6	0.088	82.3%	0.22	3.2%

nique (described in detail in Ref. 10) (Fig. 6e). Fast BVF mapping was designed to accurately estimate voxel BVF even in the presence of artifactual intensity shading caused by spatially nonuniform coil sensitivity. The method generates BVF maps at the original voxel size of the input image, similarly to the BVF mapping technique of Hwang and Wehrli (5). Trilinear interpolation was applied directly to the test images to demonstrate accuracy in the worst-case scenario. Subvoxel BVF was then estimated from the interpolated image as

$$BVF \approx 1 - I/I_{\text{marrow}} \tag{14}$$

Accuracy was assessed using error histograms and the previously-described parameters.

Application to In Vivo MR Images

To illustrate the effectiveness of the method, subvoxel processing was applied to two in vivo images of trabecular bone (Fig. 7). The images were acquired in the distal radius at  $137 \times 137 \times 350 \mu\text{m}^3$  voxel size (9,11), and were first processed with the fast BVF mapping technique. These images were subsequently subvoxel-processed, binarized, and projected to provide a visual impression of the trabecular architecture.

RESULTS AND DISCUSSION

The parameters quantifying accuracy for all the processed specimens are summarized in Tables 3 and 4, which show the mean absolute error and the percent of subvoxels assigned correct BVF. The results for infinite SNR show that 85–92% of the subvoxels were assigned correct BVF by subvoxel processing in comparison to only 26–50% using trilinear interpolation. The improvement in accuracy is even more striking at a realistic SNR of 10. Only 3–5% of

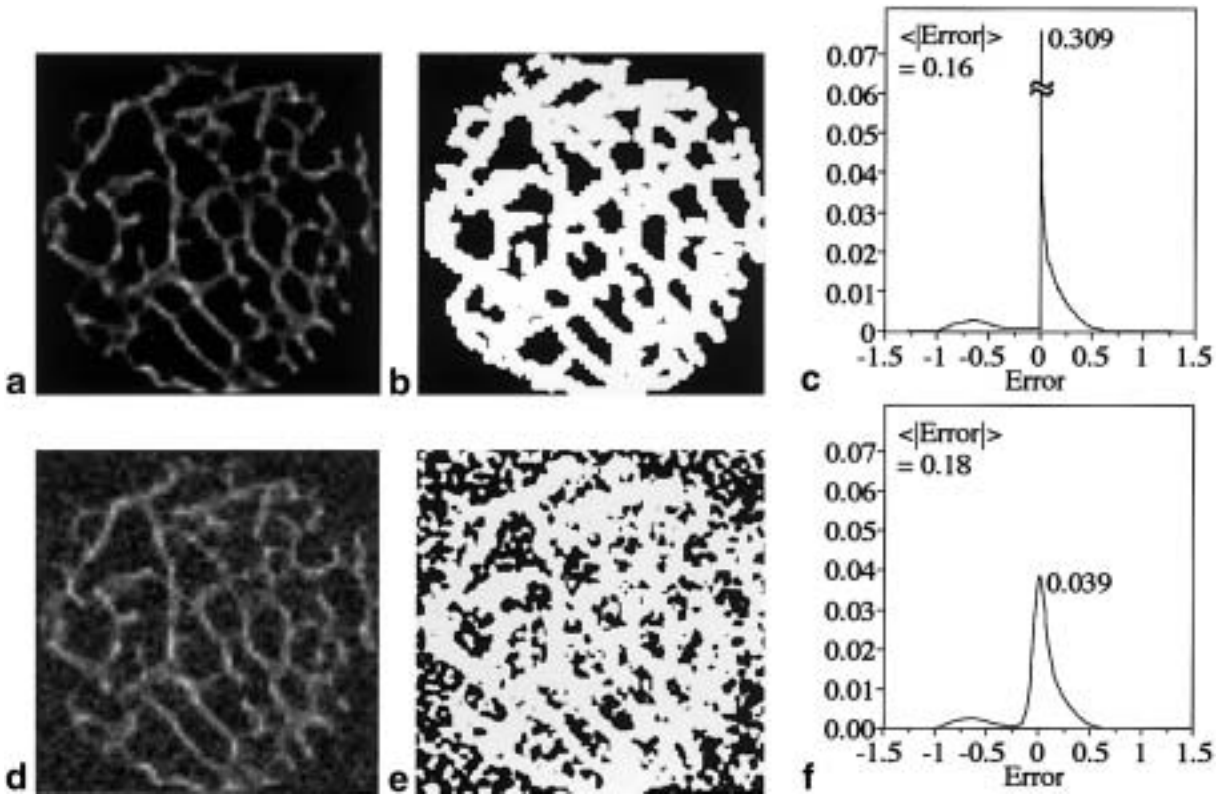


FIG. 8. Trilinear interpolation. **a**: Trilinear interpolation decreases the apparent voxel size of the low-resolution BVF map (Fig. 6c) to that of the gold standard, but the low intensities demonstrate that BVF did not increase in any of the voxels. **b**: The blurring is particularly evident when all voxels with BVF > 0 are shown in white. **c**: The histogram of error shows that only 30.9% of the subvoxels have zero error (i.e., were assigned the correct BVF) and that the average absolute error was 17.72. **d–f**: The analogous images and histogram for the result of applying trilinear interpolation to the test image with SNR = 10 (Fig. 6d). The grayscale in part d is different from the one in part a because noise results in negative values. The histogram in part f shows that <4% of the subvoxels were assigned correct BVF.

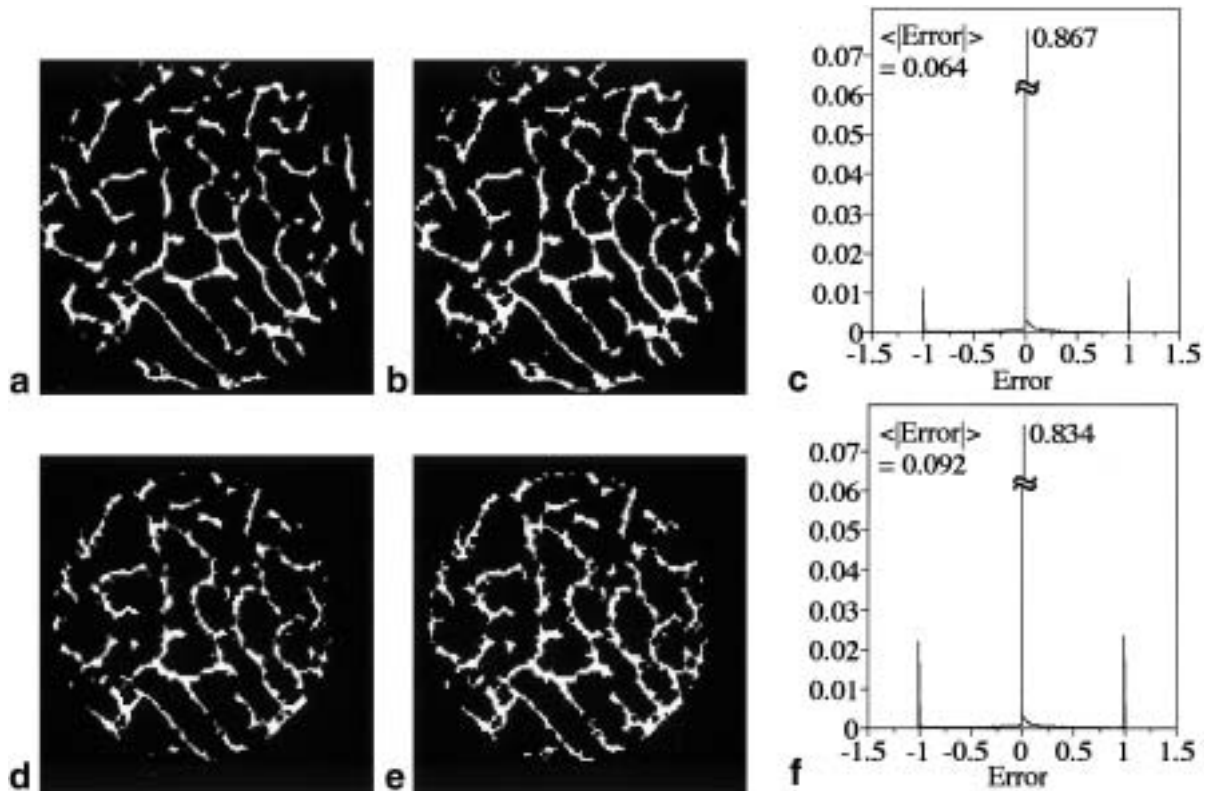


FIG. 9. Subvoxel processing. **a**: The result of applying subvoxel processing to the noiseless low-resolution BVF map in Fig. 6b demonstrates an increase in apparent resolution without blurring trabeculae. **b**: The BVF map was binarized by displaying all subvoxels with BVF > 0 in white to accentuate any blurring. The binarized image looks nearly identical to the BVF map in part **a** since blurring is essentially nonexistent. **c**: The error histogram. **d–f**: The analogous images and error histogram for the result of applying fast BVF mapping and subvoxel processing to the test image with SNR = 10 (Fig. 6d). The error histograms show that classification accuracy is very nearly the same at infinite SNR (**c**) and at SNR = 10 (**f**).

subvoxels were assigned correct BVF by trilinear interpolation. In contrast, 82–90% of the subvoxels were still assigned correct BVF by subvoxel processing. The results also show that the mean absolute error is two to three times less for subvoxel processing than for trilinear interpolation at both SNR levels.

To visually demonstrate the accuracy of subvoxel processing in comparison to trilinear interpolation, Fig. 6a shows a cross section of one of the unprocessed images while Fig. 6b–d shows the corresponding gold-standard BVF map, noiseless low-resolution BVF map, and test image with SNR = 10. Fast BVF mapping removes background noise, but there is still extensive partial volume blurring (Fig. 6e). Although trilinear interpolation produces smoother images (Fig. 8a and d), blurring is evident, especially after thresholding the BVF maps such that all voxels with BVF > 0 appear white (Fig. 8b and e). The error histograms (Fig. 8c and f) show that even in the noiseless case, the mean absolute error was 0.16 and only 31% of the subvoxels were assigned the correct BVF. At SNR = 10, fewer than 4% of the subvoxels were error-free. Furthermore, the low intensities of the BVF maps indicate that none of the voxel BVFs have increased. In contrast, the results of subvoxel processing (Fig. 9a and d) are devoid of blurring and are nearly identical to the thresholded images (Fig. 9b and e). The similarity between the gold

standard and the processed test image is striking, especially given the low resolution and SNR of the unprocessed test image (Fig. 6d).

The multiple-pass algorithm exacts a penalty in computation time. One alternative that has been investigated is the modified single-pass algorithm, which assigns primary and secondary weights during the first pass. For example, a zero primary weight may be assigned to subvoxels that do not have at least one bone-containing voxel “attracting” bone to all of its exposed sides. For example, the boundary subvoxels in Fig. 10 are assigned a primary weight of zero since they all have one side that lacks a bone-containing voxel. All the bone is thus shifted to the central subvoxels (Fig. 10). Similarly, subvoxel *d* from the first example in Fig. 1 is assigned a zero primary weight by the modified algorithm since it has no voxels attracting bone from the left. Although the modified single-pass algorithm helps keep the trabeculae from becoming diffuse, preliminary results confirm that the multiple-pass algorithm is more effective in providing a compact solution.

A demonstration of the potential of subvoxel processing for enhancing images in the low-resolution regime is given in Fig. 11, which shows 3D projections of subvoxel-processed 3D in vivo images of the human radius. The anisotropic tubular structure, suggesting a predominance of trabeculae along the direction of principal loading, is well

visualized. It should be noted that even with the most advanced technology it is currently not possible to obtain images of trabecular architecture in vivo at a resolution better than trabecular thickness. In the distal radius, voxel sizes reported by MR range from  $5.5 \times 10^{-3} \text{ mm}^3$  (9) to  $12 \times 10^{-3} \text{ mm}^3$  (3), corresponding to a mean linear resolution of 187 and 257  $\mu\text{m}$ , respectively. In peripheral quantitative CT (p-QCT) of the wrist, the smallest reported voxel size is 160  $\mu\text{m}$  (12). However, the point-spread function is considerably wider in CT than in MR, resulting in an effective resolution closer to 300  $\mu\text{m}$ . Realizing the limitations of image resolution, Majumdar et al. (3) referred to the derived histomorphometric measures as “apparent.” Müller et al. (13) demonstrated excellent serial reproducibility in histomorphometric parameters obtained in vivo in the distal radius of test subjects by p-QCT, although the reported trabecular thickness values were overestimated by at least a factor of 2. While apparent histomorphometric measures may still be useful as long as they track true variations in these parameters, analytical approaches aimed at deriving topological parameters (14–17) are unlikely to yield meaningful parameters at in vivo resolution without enhancement of the apparent resolution.

Subvoxel processing was recently applied to MR images of the distal radius in a study of 79 women with varying degrees of osteopenia (18). The subvoxel-processed bone volume fraction maps were subsequently subjected to digital topological analysis (15,16) as a means of characterizing the connectivity of the trabecular network. The resulting data showed that the structural parameters better discriminated women who had sustained vertebral fractures from those who had not.

**CONCLUSIONS**

In summary, a method has been presented that greatly alleviates the effects of partial volume blurring in tomographic images of binary systems, i.e., objects possessing only two discrete materials. The results suggest that accurate structural information for characterizing trabecular bone architecture may be possible on the basis of MR images acquired in vivo. Such information has previously only been obtainable by histomorphometry or microscopic imaging in bone specimens and biopsies. The new algorithm may therefore facilitate the noninvasive quantifica-

0	0.3	0.4
0	$\frac{0}{0.43}$	0.6
0	$\frac{0}{0.37}$	0.5

FIG. 10. Modified single-pass algorithm applied to the modified algorithm to the array of voxels shown in Fig. 1a. Since the subvoxel in the upper left corner does not have any bone towards its left side, it was assigned a primary weight of zero. In contrast to the single-pass result in Fig. 1b, the subvoxel was thus assigned BVF = 0 and its bone was partitioned among the voxels towards the center of the trabecula.

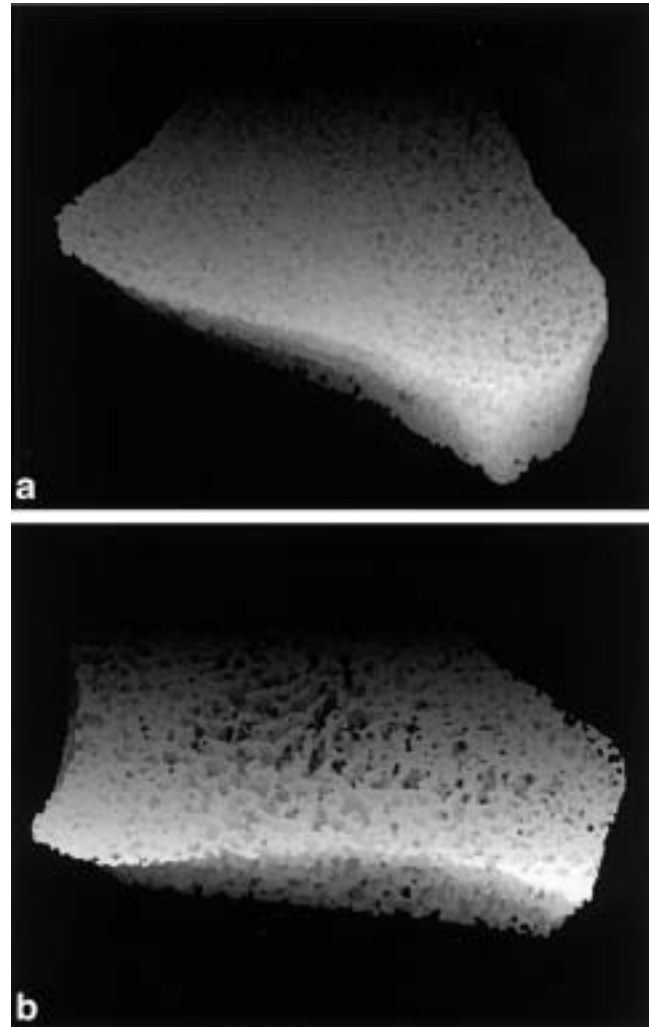


FIG. 11. 3D projections of the in vivo image shown in (a) Fig. 7a and (b) Fig. 7b following subvoxel processing. The architectural differences are evident, especially the central clearing of trabeculae in part b. The sheet-like nature of the trabeculae in b are also visualized. Parameters for quantifying these visible differences in architecture have recently been derived and applied to predict fracture risk (18).

tion of trabecular architecture for predicting fracture risk or for monitoring the efficacy of therapy.

**ACKNOWLEDGMENTS**

The authors are indebted to Dr. Laib and Prof. Peter Rueggsegger of the Institute of Biomedical Engineering at the University of Zurich and the Swiss Federal Institute of Technology Zurich (ETH Zurich), as well as Dr. Michael Thornton of the EVS Corporation, London, Ontario, for acquiring some of the  $\mu$ -CT images.

**REFERENCES**

1. Link TM, Majumdar S, Augat P, Lin JC, Newitt D, Lu Y, Lane NE, Genant HK. *In vivo* high resolution MRI of the calcaneus: differences in trabecular structure in osteoporosis patients. *J Bone Miner Res* 1998; 13:1175–1182.

2. Wehrli FW, Hwang SN, Ma J, Song HK, Ford JC, Haddad JG. Cancellous bone volume and structure in the forearm: noninvasive assessment with MR microimaging and image processing [see erratum published in *Radiology* 1998;207:833]. *Radiology* 1998;206:347–357.
3. Majumdar S, Genant HK, Grampp S, Newitt DC, Truong VH, Lin JC, Mathur A. Correlation of trabecular bone structure with age, bone mineral density, and osteoporotic status: *in vivo* studies in the distal radius using high resolution magnetic resonance imaging. *J Bone Miner Res* 1997;12:111–118.
4. Gordon CL, Webber CE, Christoforou N, Nahmias C. *In vivo* assessment of trabecular bone structure at the distal radius from high-resolution magnetic resonance images. *Med Phys* 1997;24:585–593.
5. Hwang SN, Wehrli FW. Estimating voxel volume fractions of trabecular bone on the basis of magnetic resonance images acquired *in vivo*. *Int J Imaging Syst Technol* 1999;10:186–198.
6. Wu Z, Chung H-W, Wehrli FW. A Bayesian approach to subvoxel tissue classification in NMR microscopic images of trabecular bone. *Magn Reson Med* 1994;31:302–308.
7. Hwang SN, Wehrli FW. Subvoxel processing: a new method for alleviating partial volume blurring in MR images of trabecular bone. In: *Proceedings of the 8th Annual Meeting of ISMRM, Denver, 2000*. p 2134.
8. Gudbjartsson H, Patz S. The Rician distribution of noisy MRI data. *Magn Reson Med* 1995;34:910–914.
9. Song HK, Wehrli FW. *In vivo* micro-imaging using alternating navigator echoes with applications to cancellous bone structural analysis. *Magn Reson Med* 1999;41:947–953.
10. Hwang SN, Wehrli FW. A fast method for estimating voxel bone volume fractions from *in vivo* high-resolution MR images. In: *Proceedings of the 9th Annual Meeting of ISMRM, Glasgow, Scotland, 2001*.
11. Ma J, Wehrli FW, Song HK. Fast 3D large-angle spin-echo imaging (3D FLASE). *Magn Reson Med* 1996;35:903–910.
12. Laib A, Häuselmann HJ, Rügsegger P. *In vivo* high resolution 3D-QCT of the human forearm. *Technol Health Care* 1998;6:329–337.
13. Müller R, Hildebrand T, Häuselmann HJ, Rügsegger P. *In vivo* reproducibility of three-dimensional structural properties of noninvasive bone biopsies using 3D-pQCT. *J Bone Miner Res* 1996;11:1745–1750.
14. Pothuaud L, Porion P, Lespessailles E, Benhamou CL, Levitz P. A new method for three-dimensional skeleton graph analysis of porous media: application to trabecular bone microarchitecture. *J Microsc* 2000;199:149–161.
15. Saha PK, Gomberg BR, Wehrli FW. Three-dimensional digital topological characterization of cancellous bone architecture. *Int J Imaging Syst Technol* 2000;11:81–90.
16. Gomberg BR, Saha PK, Song HK, Hwang SN, Wehrli FW. Topological analysis of trabecular bone MR images. *IEEE Trans Med Imaging* 2000;19:166–174.
17. Hildebrand T, Laib A, Muller R, Dequeker J, Ruegsegger P. Direct three-dimensional morphometric analysis of human cancellous bone: microstructural data from spine, femur, iliac crest, and calcaneus. *J Bone Miner Res* 1999;14:1167–1174.
18. Wehrli FW, Gomberg BR, Saha PK, Song HK, Hwang SN, Snyder PJ. Digital topological analysis of *in vivo* magnetic resonance microimages of trabecular bone reveals structural implications of osteoporosis. *J Bone Miner Res* 2001;16:1520–1531.